Separation of XRD peak profiles in single-phase metals with bimodal grain structure to analyze stress partitioning

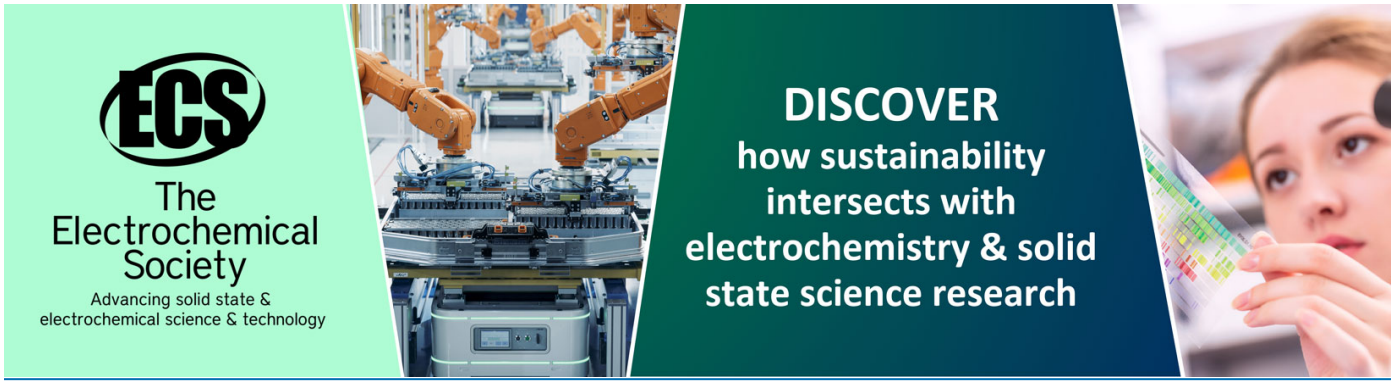

Separation of XRD peak profiles in single-phase metals with bimodal grain structure to analyze stress partitioning

E Sjögren-Levin[1], W Pantleon[2], A Ahadi[1], Z Hegedüs[3], U Lienert[3], N Tsuji[4], K Ameyama[5] and D Orlov[1]

[1] Department of Mechanical Engineering Sciences, Lund University, Lund, Sweden.
[2] Department of Civil and Mechanical Engineering, Technical University of Denmark, Kongens Lyngby, Denmark.
[3] Deutsches Elektronen-Synchrotron (DESY), Hamburg, Germany.
[4] Department of Materials Science and Engineering, Kyoto University, Kyoto, Japan.
[5] Department of Mechanical Engineering, Ritsumeikan University, Kusatsu, Japan.

E-mail: elis.sjogren@material.lth.se, dmytro.orlov@material.lth.se

Abstract. Materials with bimodal grain size distributions have an attractive combination of strength and ductility. Harmonic structure materials are a category of bimodal-structure materials with a specific microstructure design. The deformation mechanisms of such novel materials during the early stages of deformation are not well understood. Thus, we deformed nickel with harmonic structure in tension until a true strain of 0.04 while recording powder diffraction patterns with high-energy synchrotron X-rays. Line profile analysis based on such data enables quantification of stress states and lattice defect densities in different phases in multi-phase materials. Bimodal size distributions in single-phase materials add extra complexity due to the absence of differences in composition and crystal structure causing the diffraction peaks from fine and coarse grains to appear at the same diffraction angles. Therefore, prior to any meaningful line profile analysis, the respective diffraction profiles need to be separated. A general method for automatically separating profiles originating from different grain fractions in bimodal materials is presented in this work.

1. Introduction

A rapidly increasing number of studies over the past decade has demonstrated possibilities for overcoming the strength – ductility balance in single-phase materials [1]. This can be achieved by careful tailoring of heterogeneous microstructures with regions of coarse and fine grains [2, 3]. Harmonic structure (HS) materials have a special kind of heterogeneous microstructure where regions of fine grains create a continuous network (skeleton) encompassing islands of coarse grains [4, 5].

Several recent experimental [6-8] and computational [3, 9] studies have been focused on investigating the early stages of plastic deformation in HS materials to understand the mechanics of fine and coarse grains. These studies revealed that stresses and strains partition between the grain fractions from the early stages of elastic-plastic transition. However, a direct quantitative measurement of stresses was not performed. *In situ* X-ray diffraction experiments allow following the evolution of stress-state in the constituent phases of composites and alloys during mechanical tests, cf. [10]. A dedicated *in situ* X-ray diffraction experiment can capture the average elastic behavior within each fraction of coarse and fine grains, allowing direct determination of stress-partitioning in addition to microstructural features.

In the case of multi-phase materials, diffraction peaks from different phases are often easy to distinguish as they appear at different scattering angles in a diffraction pattern. For single phase materials with heterogeneous grain sizes, the separation of diffraction peaks from coarse and fine grain fractions is more complicated since they appear at the same diffraction angle. The mean grain diameters of both grain fractions are substantially higher than 1 μm in HS wherefore no significant difference in size broadening is expected between the fractions. Therefore, peak broadening-based methods such as presented in [11] cannot be applied. Furthermore, it is not possible to distinguish the different fractions from specific texture components as in [12].

In this study, we outline a procedure for tailoring the collection of X-ray diffraction data for materials with heterogeneous grain sizes along with an algorithm for separating average diffraction signals from grains of different sizes. The elastic strains of the respective grain fractions are determined and the accuracy of the algorithm is evaluated.

2. Experimental details

2.1. Material fabrication and characteristics

Nickel samples were prepared through a route of powder metallurgy by mechanical milling of nickel powder particles with average particle size of 150 μm followed by spark plasma sintering to achieve a harmonic-structure [8]. Samples for characterization by electron backscatter diffraction (EBSD) were prepared by grinding with SiC paper down to #4000 grit followed by polishing with colloidal silica. The typical characteristics of HS materials with a continuous network of fine grains surrounding islands of coarse grains is shown in figure 1a where high angle boundaries (with misorientation angles above 15°) are indicated. A reasonable threshold for separating the grain size fractions into coarse and fine is an equivalent circular diameter of 5 μm (which we will elaborate on in a future paper). Assuming such a threshold, the area fraction of fine grains below 5 μm is determined to be 24%.

Dog-bone shaped, flat tensile specimens with 7 mm gauge length and 1.5 mm width were prepared using electric discharge machining and subsequently mechanically ground to a thickness of 0.8 mm.

2.2. Experimental set-up at Petra III

In situ synchrotron X-ray data were acquired at the synchrotron radiation facility Petra III, beamline P21.2, using a beam energy of 52 keV and a beam cross-section of 100x100 μm^2 until a true strain 0.04. The sample was mounted in a custom-made screw-driven load frame equipped with a 1 kN load cell. Markers were placed at the ends of the gauge length for the measurement of macroscopic strain with an optical camera. The load frame was placed with the tensile axis horizontally on top of a diffractometer. The diffractometer allowed for translations as well as ω-rotation around the vertical axis, as indicated in figure 1b. A position-sensitive area detector (VAREX XRD4343CT) with pixel size 150x150 μm^2 and array size 2880x2880 was placed at approximately 1.5 m downstream of the specimen to cover the first six Debye-Scherrer rings of nickel. The detector position and tilt were calibrated with a NIST SRM660c standard LaB_6 powder using Fit2D software.

2.3. Experimental procedure

Before commencing tensile loading, the specimen was translated such that the position of a reference grain in the gauge section of the specimen coincided with the rotation center of the diffractometer. Furthermore, this grain was fully illuminated by the beam and had its 400 reflection parallel with the tensile axis. The tensile loading was conducted stepwise with 10-20 MPa stress increments. During loading, the detectors were capturing images continuously for keeping the selected reference grain in the beam. This ensured the illumination of approximately the same specimen volume throughout the experiment. After each load step, the reference grain was re-centered. For data acquisition, the specimen was rotated 1° in 50 intervals of 0.02° around the ω-axis perpendicular to the load axis. Optical images were acquired after each loading step for subsequent digital image correlation to determine the strain.

The beam cross-section of 100x100 μm^2 was selected based on two criteria. The beam needs to be sufficiently large to fully illuminate grains over the entire range of sizes, but small enough to not capture

a too high number of coarse grains. Figure 1c depicts one ω-interval of a diffraction pattern corresponding to the Debye-Scherrer ring 111. It can be seen that the pattern constitutes of a continuous ring of low intensity and many overlaying high-intensity diffraction spots. The ring has an appearance similar to that of partially recrystallized cold rolled samples [12-14]. In those studies, the diffraction spots were associated with growing grains, and the continuous ring with a deformed matrix. Thus, in the present study we assume that diffraction spots and continuous rings represent coarse and fine grain fractions, respectively. The use of a larger beam size would result in a diffraction pattern of mostly high-intensity spots. To evaluate the mechanical behavior of the two grain fractions separately, their respective diffraction patterns need to be separated. To capture full diffraction spots from individual grains and allow them to be separated, the data are acquired in small ω-intervals while rocking over ω.

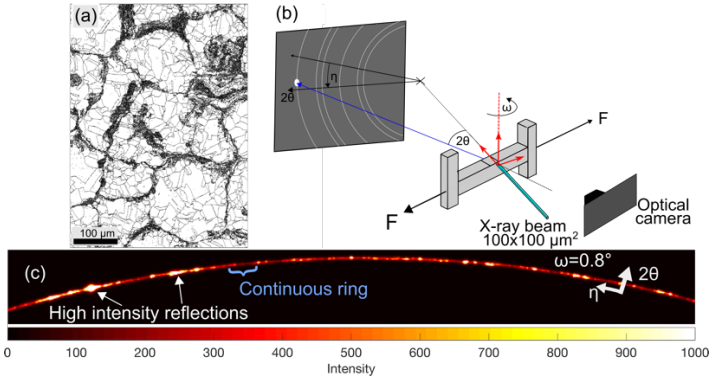

Figure 1: (a) High angle boundary map obtained by ESBD showing a representative overview of harmonic structure nickel. (b) Schematic of the experimental set-up. (c) Typical section of the first Debye-Scherrer ring for one specific ω-interval showing an arc in η of about 30°. Note that on the Debye-Scherrer ring, high-intensity diffraction spots originate from coarse grains, while the continuous ring of low intensity originates from fine grains.

3. Data analysis

3.1. Algorithm for peak separation

The algorithm for separating the diffraction patterns according to the fractions of different grains was developed and realized as a MATLAB® script. The algorithm merely defines a threshold in intensity between the diffraction spots and the continuous Debye-Scherrer rings in a range of [2θ, η, ω]. The recorded intensity may vary among diffraction patterns acquired at different load increments due to variation in beam intensity and acquisition time. Moreover, the recorded intensity varies with peak position (on the detector) depending on Lorentz factor. Therefore, the separation procedure was carried out on the diffraction patterns acquired at each load increment and diffraction ring separately. The entire separation procedure for the 111 ring is presented as an illustrative example. Note, only grains with <hkl> along the tensile axis within a range of ± 15° in η-direction (figure 2a) are of interest in this study.

Step 1: From the recorded diffraction pattern, a 3D intensity distribution is extracted for each ring in an interval [$2\theta_{hkl}$-$2\theta_{full}$…$2\theta_{hkl}$+$2\theta_{full}$, -15°…15°, 0°...1°] with large $2\theta_{full}$ to separate hkl rings (figure 2a).

Step 2: A 1D azimuthal distribution along η is obtained by integrating 2θ and ω (figure 2b). From this, high-intensity peaks are identified and ranked according to their maximum intensity. Simultaneously their positions of maximum intensity η_{max} and their η ranges are determined from the intensity minima between them. The most intense peak at η^1_{max} having a range η^1_{max}-η^1_{low}…η^1_{max}+η^1_{high} is shown in figure 2c.

Step3: To optimize further analysis, the 2θ range is now limited based on the most intense peak. Azimuthal integration is performed in η and ω in the range [η^1_{max}-η^1_{low}…η^1_{max}+η^1_{high},0°...1°] to obtain a radial profile (still not background corrected). The full width at half maximum intensity (FWHM) of the profile in 2θ is determined and used to limit the 2θ range to [$2\theta_{hkl}$ -10*$2\theta_{FWHM}$…$2\theta_{hkl}$ +10*$2\theta_{FWHM}$]. This smaller 2θ range (indicated by dashed box in the inset in figure 2c) still comprises the most intense peak while keeping the region to investigate smaller.

Step 4: For further quantification the intensity background is determined as average in the combined 2θ range [$2\theta_{hkl}$ -15*$2\theta_{FWHM}$…$2\theta_{hkl}$ -10*$2\theta_{FWHM}$] and [$2\theta_{hkl}$ +10*$2\theta_{FWHM}$…$2\theta_{hkl}$ +15*$2\theta_{FWHM}$] and subtracted from the 3D intensity distribution [$2\theta_{hkl}$ -10*$2\theta_{FWHM}$…$2\theta_{hkl}$ +10*$2\theta_{FWHM}$, -15°…15°, 0°...1°].

Step 5: For each peak identified from the azimuthal distribution along η, a 1D azimuthal distribution along the angle ω is obtained by integrating 2θ over $[2\theta_{hkl}\text{-}10*2\theta_{FWHM} \ldots 2\theta_{hkl}\text{+}10*2\theta_{FWHM}]$ and η over $[\eta_{max} - \eta_{low} \ldots \eta_{max} + \eta_{high}]$. The intensity distribution varies significantly along both azimuthal directions due to the individual coarse grains giving rise to high intensity peaks at certain (η, ω) positions. The contribution of the finer grains is rather smooth and assumed to be an almost constant function in η and ω. When normalizing the intensity by the integration range ($\Delta\eta = \eta_{high}$ - η_{low}, $\Delta\omega = 0.02°$), fine grains are assumed to contribute a constant normalized intensity level.

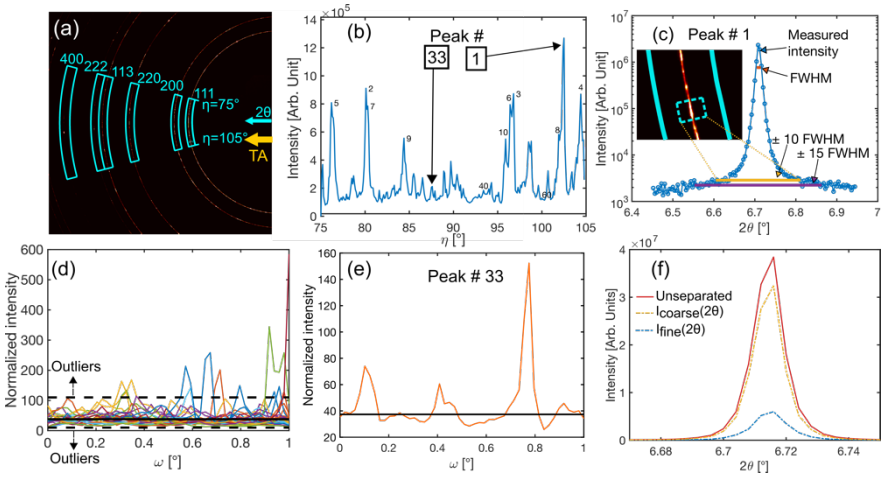

Figure 2: Illustration of the critical steps explained in the main text of the separation of high-intensity spots from the continuous ring in diffraction data.

Step 6: The constant normalized intensity level to be used as threshold is defined by selecting the 25 peaks recognized along η with lowest maximum integrated intensity to represent regions outside pronounced high intensity peaks. These 25 peaks correspond to rather small grains. Consequently, their average normalized intensity $I_{norm,thr}$ defines a suitable threshold for distinguishing between fine grains contributing to continuous rings with low variation in η and ω and coarse grains giving rise to individual high intensity peaks. The 25 profiles in ω (figure 2d) may still contain high-intensity peaks. For removing them, the profiles are inspected individually, and recognized outliers removed from analysis.

Step 7: Based on the threshold value for the normalized intensity $I_{norm,thr}$, an azimuthal threshold $I_{thr} = I_{norm,thr} * \Delta\eta * \Delta\omega$ is established. With that azimuthal threshold, the azimuthal range for each ring is separated in two regions depending on whether the (background corrected) intensity exceeds the threshold value (region A) or not (region B). Figure 2e displays the ω-profile of a peak with low intensity but still high enough to be part of the region of pronounced high intensity peaks. Intensities higher than the azimuthal threshold indicated by the horizontal line correspond to region A and lower to region B.

Step 8: The intensity distribution of the latter region B (for which the radially integrated intensity does not exceed the threshold) is attributed to solely fine grains. The corresponding radial profile $I_B(2\theta)=I_{fine}(2\theta)$ from these azimuthal regions is derived and analyzed. The intensity distribution of region A (i.e. from all the regions exceeding the threshold) contain diffraction signal from coarse grains and fine grains of e.g. same orientation diffracting at the same azimuthal angles. The determined radial profile $I_A(2\theta) = f_{A,coarse}\ I_{coarse}(2\theta) + (1\text{-}f_{A,coarse})\ I_{fine}(2\theta)$ is a superposition of two profiles from fine and coarse grains which can be separated presuming that the fine grains contribute with the same profile $I_{fine}(2\theta)=I_B(2\theta)$ as in region B $I_{coarse}(2\theta) = (f_{A,coarse})^{(-1)}\ (I_A(2\theta) - (1\text{-}f_{A,coarse})\ I_B(2\theta))$ (figure 2f). The fraction of coarse grains $f_{A,coarse}$ contributing in region A is obtained from the ratio between the integrated intensities above the threshold and the entire integrated intensity. The radial profile of the fine grains in the full azimuthal region (η, ω) [-15°… +15°, 0°…1°] is given by $I_{fine}(2\theta) = I_B(2\theta) + (f_{A,coarse})\ I_B(2\theta)$ (figure 2f).

In this manner, the average radial profiles of the grain fractions are obtained which are of interest for the present study. If analysis of individual coarse grains is attempted, their corresponding individual high-intensity peaks within the intensity distribution (of region A) are to be identified by projecting the intensity along 2θ on the azimuthal plane (η, ω). The relevant ranges in the azimuthal angles of

individual high-intensity peaks can be determined and individual radial profiles constructed. However, details of the analysis of individual coarse grains are outside of the scope of this paper.

3.2. Radial profiles

The separated and unseparated radial profiles are characterized in terms of average peak positions and total intensities. Intensities above 1/50 of the maximum intensity constitute the corresponding peaks, and the average peak position ($2\theta_{mean}$) is calculated as the weighted average based on these intensities. The peak position relates to the average spacing d_{hkl} of diffracting {hkl} lattice planes and the wavelength λ through Bragg's law $\lambda = 2d\sin(\theta)$. The total intensities in the separated profiles correspond to the total diffracting volume of coarse and fine grains.

4. Results & Discussion

Diffraction patterns were acquired during interruptions of the tensile test at certain macroscopic stress values as indicated in figure 3a. Strain values at each loading step were obtained by digital image correlation from optical images using the GOM Correlate commercial software. The outlined algorithm was applied to separate diffraction signals from coarse and fine grains. The ratio between the total intensity from the fine grains and the total intensity from the entire diffracting volume, i.e. the volume fraction of fine grains, for the first four Debye-Scherrer rings at the unloaded state were 17.4% <111>, 18.7% <200>, 24.9% <220> and 26.7% <311> with an average fraction of fine grains of 22%. As the used threshold I_{thr} value is based on the average intensity level of the continuous ring (or better the 25 identifiable peak of lowest integrated intensity) it is *a priori* unknown to which threshold value d_{thr} in terms of grain size this corresponds. Comparing the obtained volume fraction of fine grains with the finding from orientation maps obtained by EBSD on the same material that grains smaller than 5 μm contribute an area fraction of 24 %, it is reasonable to presume that the algorithm discriminates grains larger and smaller than 5 μm into coarse and fine grain fraction, respectively. The threshold value d_{thr} of 5 μm and its stability is further evaluated by checking the fraction of fine grains with increasing strain.

The lattice strains $\varepsilon_{hkl}=(d_{hkl}-d^0_{hkl})/d^0_{hkl}$ of grain families with four different <hkl> along the tensile direction are calculated based on the first four Debye-Scherrer rings. The stress-free $2\theta_{mean}$ position ($2\theta^0_{mean}$) was evaluated at 0% strain for the unseparated and separated profiles, and the $2\theta_{mean}$ was calculated for the subsequent stress increments. Figure 3b shows the variation of lattice strain with true stress for grains with tensile axis along <111> obtained from the first Debye Scherrer ring. The three different curves represent the average lattice strain from the unseparated profile and for the two different grain fractions separately. With increasing macroscopic stress and strain, all elastic lattice strains increase, but the fine grain fraction develops larger elastic strains then the coarse-grained fraction indicating the development of internal stresses and stress partitioning. Where forward stresses occur in the fine grains and back stresses develop in the coarse grains. The details of the stress partitioning and the yielding of the harmonic structure will be presented in a forthcoming paper.

Figure 3c presents the evolution of the fraction of fine grains with macroscopic strain based on the ratio of integrated intensity of fine grains to the total intensity. For all grain families, the fraction of fine grains increases with strain. This might be a consequence of coarse grains getting subdivided by deformation-induced dislocation boundaries due to plastic yielding. The developing mosaicity leads the diffraction spots to spread in the azimuthal directions (η, ω). This causes the smooth continuous ring to comprise of a combination of intensity from fine grains and parts of high-intensity spots from subgrains in deformed coarse grains. At approximately 0.01 true strain, the continuous ring intensity starts to increase relative to the strongest high-intensity spots, which results in a higher f_{fine} and an increase of d_{thr}. Furthermore, the superposition of intensities of fine grains and subgrains from coarse grains causes the lattice strains of the fine-grained fraction to be underestimated. It is also noted, that the fraction of fine grains is always largest for grains with one of their <311> directions along the tensile axis followed by <220>, <200> and <111>. This might not be a real effect, but an artefact of the separation algorithm and the used threshold for separating fine and coarse grains. In particular rings with a high multiplicity

will have a plentitude of high-intensity peaks, which makes their discrimination difficult. Overlapping peaks will be attributed to the smooth intensity distribution causing a higher fraction of fine grains.

In summary, the algorithm separates the diffraction signals from coarse and fine grains nicely at the targeted threshold d_{thr} of 5 µm until 0.01 true strain. Afterwards, the effective threshold d_{thr} increases and as a consequence, the lattice strains of the initial fine-grained fraction are not monitored properly anymore as part of the coarse grains become merged into the fine-grained fraction.

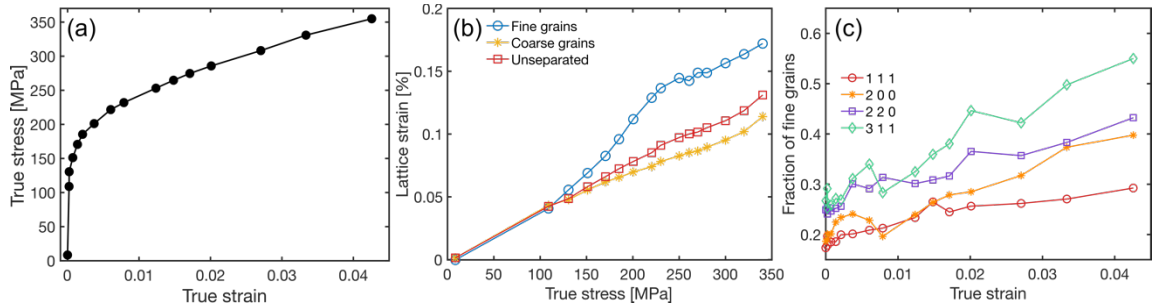

Figure 3: (a) Macroscopic stress strain curve. (b) Lattice strain of 111 ring for separated and unseparated profiles with true stress. (c) Fraction of fine grains with true strain according to separation algorithm.

5. Conclusion

In situ X-ray diffraction was carried out during tensile deformation of harmonic structured nickel with bimodal grain size distribution until 0.04 true strain. The settings for acquisition were adjusted such that azimuthal segments from coarse and fine grains were distinguishable. An algorithm for automatic separation of radial profiles of respective grain fractions was developed. The fraction of fine grains (with diameters below 5 µm) is accurately monitored until approximately 0.01 true strain. Then the diffraction signal from the coarse grains partially merges with the signal from fine grains. The average elastic strains of the two grain fractions differ during tensile deformation revealing stress partitioning.

Acknowledgements

The authors thank the financial support by the Swedish Research Council through research grant # 2016-03811, the Swedish Foundation for International Cooperation in Research and Higher Education (STINT) grants # SJ2017-7432 and MG2019-8450, and Interreg program “ESS & MAX IV: Cross Border Science and Society”, grants DTU007 and LU070. We acknowledge DESY (Hamburg, Germany), a member of the Helmholtz Association HGF, for the provision of experimental facilities. Parts of this research were carried out at PETRA III. Beam time at beamline P21.2 was allocated for proposal I-20190991 EC and has been supported by the project CALIPSOplus under the Grant Agreement 730872 from the EU Framework Programme for Research and Innovation HORIZON 2020.

References

[1] Y. Zhu *et al* 2021 *Mater. Res. Lett.* **9** 1-31
[2] X. Wu and Y. Zhu 2017 *Mater. Res. Lett.* 1-6
[3] A. Shokry, A. Ahadi, P. Ståhle and D. Orlov 2021 *Sci. Rep.* **11** 17445
[4] K. Ameyama *et al* 2022 *Mater. Res. Lett.* **10** 440-71
[5] D. Orlov and K. Ameyama 2020 *Mater. Sci. and Technol.* **36** 517-26
[6] D. Orlov, H. Fujiwara and K. Ameyama 2013 *Mater. Trans.* **54** 1549-53
[7] H.K. Park *et al* 2018 *Mater. Res. Lett.* **6** 261-7
[8] D. Orlov *et al* 2019 *IOP Conf. Ser. Mater. Sci. Eng.* **580** 012019
[9] D. Orlov, R. Kulagin and Y. Beygelzimer 2020 *Mater. Lett.* **275** 128126
[10] H. Van Swygenhoven and S. Van Petegem 2013 *Mater. Charact.* **78** 47-59
[11] Z. Matěj *et al* 2014 *Powder Diffr.* **29** S35-S41
[12] F.X. Lin *et al* 2015 *Philos.Mag.* **95** 2427-49
[13] E.M. Lauridsen, D.J. Jensen, H.F. Poulsen and U. Lienert 2000 *Scr. Mater.* **43** 561-6
[14] Y.D. Wang *et al* 2002 *J. Appl. Crystallogr.* **35** 684